# Probing Membrane Order and Topography in Supported Lipid Bilayers by Combined Polarized Total Internal Reflection Fluorescence-Atomic Force Microscopy

John Oreopoulos and Christopher M. Yip*
Institute of Biomaterials and Biomedical Engineering, Terrence Donnelly Centre for Cellular and Biomolecular Research, University of Toronto, Toronto, Canada

ABSTRACT Determining the local structure, dynamics, and conformational requirements for protein-protein and protein-lipid interactions in membranes is critical to understanding biological processes ranging from signaling to the translocating and membranolytic action of antimicrobial peptides. We report here the application of a combined polarized total internal reflection fluorescence microscopy-in situ atomic force microscopy platform. This platform's ability to image membrane orientational order was demonstrated on DOPC/DSPC/cholesterol model membranes containing the fluorescent membrane probe, DiI-$C_{20}$ or BODIPY-PC. Spatially resolved order parameters and fluorophore tilt angles extracted from the polarized total internal reflection fluorescence microscopy images were in good agreement with the topographical details resolved by in situ atomic force microscopy, portending use of this technique for high-resolution characterization of membrane domain structures and peptide-membrane interactions.

## INTRODUCTION

Identifying and characterizing the inter- and intramolecular interactions that govern the assembly and function of molecules within and at membrane interfaces is critical to understanding the basics of cell signaling, cell-cell interactions, and molecular transport. Toxins may exert their influence through pore complexes or other mechanisms of membrane disruption. Antimicrobial or cell-penetrating peptides necessarily need to pass through the membrane to exert their action. Intrinsic membrane proteins may require specific intermolecular interactions with specific lipids or other membrane components or structures to exert their function. Indeed, fundamental questions remain as to the underlying mechanisms associated with the formation, dynamics, and compositional variance of lipid microdomains, or so-called membrane rafts (1–10).

To date, fluorescence-based imaging techniques have proven to be among the most powerful approaches for examining membrane structure, phase separation, and domain dynamics (11–26). However, it is becoming increasingly evident that new forms of quantitative imaging that improve spatial and/or temporal resolution, provide new contrast mechanisms, or combine complementary imaging modalities are needed to further our understanding of microdomains and related membrane protein-lipid interactions (27). Examples of emerging imaging techniques to study membranes include: fluorescence lifetime imaging (28), fluorescence interference contrast microscopy (29), coherent anti-Stokes Raman scattering microscopy (30), secondary ion mass spectrometry imaging (31), and other super-resolution modes of optical microscopy (32,33). A compelling argument can also be made for the application of correlated approaches that combine two or more imaging techniques—so-called combinatorial microscopy (34). We and others have shown that coupled fluorescence and atomic force microscopy (AFM) is a useful approach for examining fundamental lipid-lipid and lipid-protein interactions in model membranes and live cells (35–43). Our studies of peptide-induced membrane remodeling prompted us to consider strategies that would provide additional insights into the effect of these peptides on membrane structure (44). For example, while coupled fluorescence and atomic force microscopy is effective for mapping the distribution of fluorescently labeled lipids and proteins against topography, these platforms are not typically configured for assessing molecular orientation or conformation, especially in the case of molecules that insert into the membrane's hydrophobic core. Furthermore, the function of membrane-associated molecules is intrinsically linked to their structure and orientation in the membrane. One means of assessing their orientational order is through a time- and ensemble-averaged quantity known as the order parameter, $\langle P_2 \rangle$ (45–54). Order parameters can be obtained via a number of orientation-sensitive techniques: Optical birefringence, ultraviolet-visible linear dichroism spectroscopy, polarized attenuated total internal reflection Fourier transform infrared (pATR-FTIR) spectroscopy, polarized Raman spectroscopy, electron spin resonance spectroscopy, nuclear magnetic resonance spectroscopy (NMR), wide angle x-ray scattering, and time-resolved fluorescence polarization anisotropy. The main differences among these techniques arise from the type of dipolar interactions that are probed, the number of order parameters that can be accessed, and the characteristic timescale of the measurement. Order parameter measurements have been critical to the study of membrane structure and dynamics (10,55,56), and in particular the effect of membrane-associated proteins. For membranes, order is usually described by the carbon-deuterium

*Submitted August 25, 2008, and accepted for publication November 17, 2008.*

*Correspondence: christopher.yip@utoronto.ca

Editor: Enrico Gratton.



0006-3495/09/03/1970/15 $2.00

doi: 10.1016/j.bpj.2008.11.041

NMR order parameter ($S_{CD}$), the measurement of which has been important to our understanding of the molecular dynamics and phase behavior of lipids and cholesterols in oriented model membranes (10,23,56–64). Recently, fluorescence polarization anisotropy was used to characterize the effect of cholesterol on the phase state and ordering of naturally occurring lipids using liposomes derived from membrane extracts of RBL-2H3 mast cells (55).

Techniques based on polarized fluorescence imaging are providing valuable insights into the molecular order and fluidity of membrane nanostructures, both in vitro and in vivo (12,65–79). These techniques exploit the dichroic absorption and/or the anisotropic emission of polarized light by fluorescent lipids or proteins to spatially detect and infer their orientation, organization, conformation, and rotational mobility. We report here the design and implementation of a combinatorial microscopy platform that integrates polarized total internal reflection fluorescence microscopy (pTIRFM) (80,81) with in situ AFM (36,82,83). This correlated imaging modality allows us to now directly map local variations in fluorescent probe orientational order inferred by pTIRFM against topographical features observed by AFM. Spatially resolved (diffraction-limited) orientation imaging was demonstrated on dioleoylphosphatidylcholine (DOPC)/distearoylphosphatidylcholine (DSPC)/cholesterol model membranes containing the fluorescent membrane probe DiI-$C_{20}$ or BODIPY-PC. Order parameters and fluorophore tilt angles (Appendix B) extracted from the pTIRFM images were in good agreement with the topographical details resolved by in situ AFM, portending the application of this technique for high-resolution characterization of membrane domain structures and peptide-membrane interactions, and in particular, the dynamics and mechanisms of antimicrobial peptide and toxin activity (36,37), and protein-induced membrane restructuring (35).

## Polarized total internal reflection fluorescence microscopy

When light passes through a material with a high refractive index, $n_2$, into another medium with a low refractive index, $n_1$, the amount of light transmitted through and reflected by the interface is dependent on both indices of refraction, as well as the beam's incident angle on the interface, $\alpha$. At internal angles of incidence equal to or greater than the critical angle, $\alpha_c$, as defined by Snell's law, total internal reflection (TIR) of the incident beam occurs, creating a surface-traveling electromagnetic wave, or evanescent field/wave that penetrates into the lower index medium with exponentially decaying intensity in a direction away from the interface (84). Since the evanescent field is confined to an extremely thin region (typically 200 nm or less) just above the substrate-sample solution interface, TIRFM is well suited for illuminating and imaging interfacial phenomena with an axial resolution that surpasses conventional confocal microscopy. Both prism- and objective-based TIRFM designs have been applied to study a wide range of cellular processes, including cell adhesion and exocytosis (81,85–89). AFM can be easily combined with an objective-based TIRFM design in which a laser beam is focused onto the back-focal plane of the microscope and positioned on the periphery of a high numerical aperture (NA) microscope objective (Fig. 1 *A*). In this configuration, the AFM would be accessing the sample from above, typically in a tip-scanning mode, while

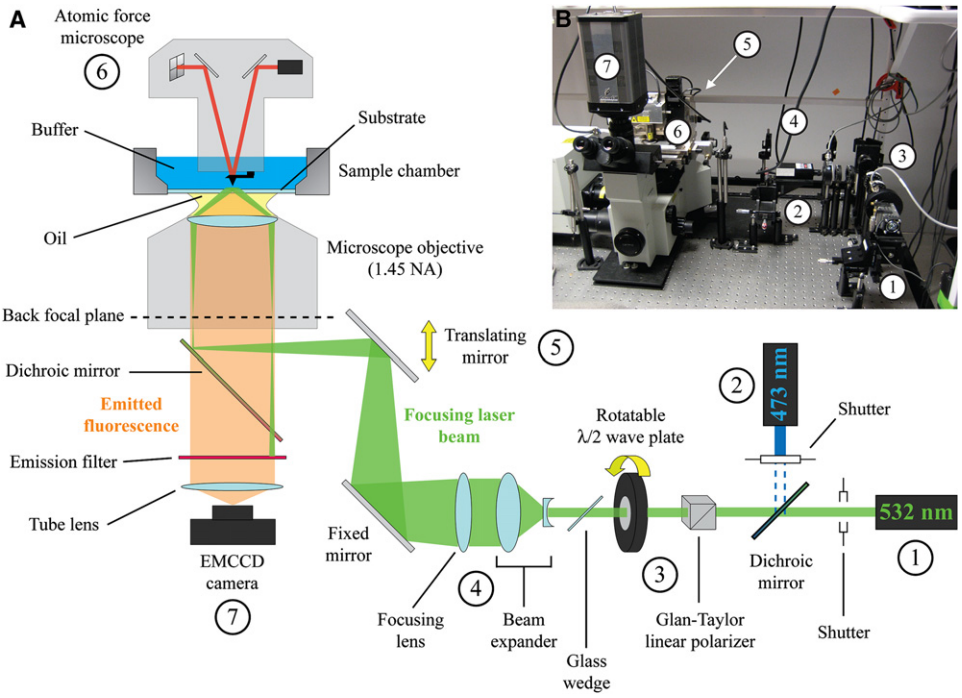


FIGURE 1 Schematic (*A*) and digital photograph (*B*) of the pTIRFM/AFM instrument. See text for details on the optical components and their arrangement. The numbered circles in panel *B* correspond to the regions of the optical train also labeled in panel *A* by numbered circles.

fluorescence can be simultaneously or sequentially acquired through the sample substrate from below by TIRFM.

When molecules are exposed to polarized light, photon absorption is dependent on both molecular structure and orientation with respect to the polarization axis. In the case of biological systems, this property allows the orientation and rotational mobility (i.e.: the orientational order) of membrane components to be determined from polarized light measurements. In TIRF, the evanescent field has unique photoselection properties that allow one to probe the time- and ensemble-averaged orientational order of a collection of fluorescent molecules embedded in a two-dimensional medium by examining the dichroism of fluorescence as a function of the illuminating light's polarization angle, $\psi$. Fluorescent molecules with absorption dipoles oriented at different tilts relative to the substrate normal are preferentially excited if the electric field vector of the evanescent wave is inclined at the same projected polar angle as the absorption dipole.

In a pTIRFM imaging experiment, by measuring the fluorescence intensity of a region of interest (ROI) as a function of the evanescent field's polarization angle ($\psi$), it is then possible to estimate the average molecular order of the fluorescent probes located within the ROI. To do so however, requires understanding how the fluorescent signal should behave under different fluorophore orientation conditions. A generalized theory of pTIRF has been developed for uniaxial (cylindrical symmetry) conditions (see Appendix A and (80) for details). The normalized, steady-state fluorescence intensity as a function of the evanescent wave's polarization angle, $\Im(\psi)$, is given by

$$\Im(\psi) = 1 + B\left(\cos^2\psi - \cos^2\psi_0\right), \tag{1}$$

where $\psi_0$ is the experimentally determined polarization angle at which $\Im(\psi)$ is a maximum (restricted to 0° or 90° for uniaxial symmetry), $B$ describes the distribution of fluorophore orientations within the detection volume, and is related to the pTIRF $\langle P_2\rangle$ order parameter by

$$B = \frac{\left(I_z - I_y + I_x\right) + \langle P_2\rangle\left(2I_z + I_y - I_x\right)}{I_y(1 - \langle P_2\rangle) + \cos^2\psi_0\left[\left(I_z - I_y + I_x\right) + \langle P_2\rangle\left(2I_z + I_y - I_x\right)\right]}, \tag{2}$$

where $I_x$, $I_y$, and $I_z$ are the evanescent field intensity directional components, which can be calculated when the relative index of refraction of the interfacial system ($n = n_1/n_2$) and the illumination beam angle of incidence ($\alpha$) are known.

From these expressions, an experimental determination of $B$ from $\Im(\psi)$ leads to a quantitative assessment of $\langle P_2\rangle$ for the fluorescent species in the ROI. It is important to stress, however, that optical polarization methods like pTIRF can only characterize the average orientation and motional freedom associated with the absorption transition moment of the fluorophore linked to a parent molecule. Relating the orientational order of the parent molecule to the orientational order of the fluorophore by this measurement can be nontrivial.

We have adapted this same formalism to our objective-based pTIRFM/AFM microscope configuration. pTIRFM images of the same field of view are captured by an electron-multiplying charge-coupled device (EMCCD) camera as $\psi$ is increased from 0° ($p$-polarized) to 90° ($s$-polarized), generating a $\psi$-image stack. This image stack can then be processed on a per-pixel basis to evaluate $\Im(\psi)$ and $B$ using Eq. 2. From these data, a spatial map of $\langle P_2\rangle$, or order parameter image, can be created and compared to an AFM topography image of the same ROI.

## MATERIALS AND METHODS

### Construction of the pTIRFM/AFM platform

A list of vendor product numbers for certain instrument parts is provided in accompanying Supporting Material. The pTIRFM/AFM instrument was modified from the platform described earlier (35,36) (Fig. 1). The instrument consisted of a Digital Instruments (Veeco, Santa Barbara, CA) Nanoscope IIIa Bioscope AFM mounted on an Olympus IX70 inverted microscope (Olympus Canada, Markham, Ontario, Canada) with objective-based total internal reflection fluorescence optics (Olympus Canada, PLAN-APO 60× objective, 1.45 NA) and an additional 1.5× image magnification lens built into the microscope frame. Several key modifications were made to the optical microscope's excitation pathway to permit polarized TIRF illumination of the sample. First, the optical fiber-launched laser was replaced with free-space launched 532 nm and 473 nm diode-pumped solid-state lasers (Extreme Lasers, Seabrook, TX) mounted to a vibration-isolated optical table with translating and tilting stages (Thorlabs, Newton, NJ). A dichroic mirror (Thorlabs) oriented at 45° relative to both laser beams allowed both beams to travel down the same optical path. Switching between the two lasers was achieved with two Uniblitz shutters (Vincent Associates, Rochester, NY) mounted in front of both laser apertures and controlled by the image acquisition software. The excitation laser beam was passed through a fixed visible wavelength Glan-Taylor linear polarizer prism and an achromatic half-waveplate, which, when rotated properly (84), allows the electric field vector defining the polarization angle of the excitation beam, $\psi$, to be set to any angle between 0° and 90°. The half-waveplate was held in a motorized rotation mount (Newport Corporation, Irvine, CA) controlled by a motion controller through custom software (National Instruments, Austin, TX, LabView, Ver. 7.0). The half-waveplate rotation angle could be set to within ±0.003°. The polarizer and half-waveplate were aligned to the parallel and perpendicular directions of the optical bench and microscope stage using the method described by Lakowicz (90). A 170-$\mu$m-thick glass wedge was oriented in the pathway after the half-waveplate such that the laser intensity, when measured at the microscope objective with a laser power meter, was nearly equal (<3% variation) for all values of $\psi$. This particular optical adjustment is crucial for quantitative fluorescence polarization microscopy (66). A series of three properly spaced lenses expanded the laser beam into a 3/4″ diameter collimated beam and focused it onto the back-focal plane of the microscope objective after reflecting off the microscope filter cube's dichroic mirror (473 nm excitation laser/505 nm cut-on wavelength dichroic mirror or 532 nm excitation laser/565

nm cut-on wavelength dichroic mirror). The illumination spot at the substrate-sample interface was ~90 $\mu$m in diameter (see Fig. 3 *A*). While larger or smaller illumination spot sizes could be obtained by selecting appropriate focal length lenses and arranging the optical elements accordingly, due to space restrictions, we were limited to a combination and arrangement of lenses that resulted in an ~90-$\mu$m diameter spot. This illumination area readily accommodated the 20 $\mu$m $\times$ 20 $\mu$m AFM scans that were performed in the centermost region of the spot. The laser polarization extinction ratio (PER) was measured using a second identical linear polarizer and a laser power meter placed at the objective (91). With a blank glass substrate chamber filled with buffer solution in place and in focus on the microscope stage, the PER was 127:1. When blank mica-glass substrates were used, a PER value of 120:1, with ~1% variation between substrates, was obtained. While the slightly lower PER for the mica-glass substrates suggests a slight depolarization of the light by the mica, it also indicates that linear polarization is well maintained through the microscope's excitation optics and remained sufficiently high for pTIRFM experiments. A manual translating mirror allowed the focused laser beam to be moved radially from the center of the objective aperture (polarized epifluorescence mode) toward the periphery (pTIRFM mode) to meet the TIR condition. The critical angle, $\alpha_c$, for the substrate-solution interface was determined by the visual disappearance of the laser beam at the objective and by observing the position of the focused laser spot in the back-focal plane of the objective with a Bertrand lens. It could also be located by the sudden disappearance of free-floating vesicles in solution above the bilayer in the camera preview mode of the image acquisition software. Since x-ray diffraction studies of supported lipid bilayers have shown that an ~1–2 nm thick water layer separates the membrane from the substrate (92,93), TIR is expected to occur at the substrate/water interface. In our experiments, freshly cleaved mica substrates were optically coupled to glass coverslips with the angle of incidence set to or just beyond the substrate/water interface critical angle of 60°. Fluorescence emanating from the sample was collected by the objective lens and imaged through a bandpass interference filter housed in the microscope filter cube (473 nm excitation; 500–550 nm bandpass, 532 nm excitation; 565–605 nm bandpass). All pTIRFM images were captured using a Photometrics (Tucson, AZ, Cascade II EMCCD camera (512 $\times$ 512 pixels, 16 $\times$ 16 $\mu$m pixel size) using Media Cybernetics (Bethesda, MD) ImagePro Plus Ver. 6.0 image acquisition software. The lateral back-projected pixel dimensions of the camera at the optical microscope sample plane was 178 $\times$ 178 nm, which was close to the optimum Nyquist sampling rate of 100 $\times$ 100 nm (94). Therefore, all optical images presented here are slightly undersampled.

## pTIRFM/AFM image acquisition and analysis

The pTIRFM/AFM image acquisition protocol was as follows: a sample ROI was brought into focus and a stack of 10 pTIRFM images was captured, incrementing $\psi$ in 10° steps from *p*- to *s*-polarization for each successive image. In Appendix C, we show that the minimum number of images to collect in a pTIRFM study of a uniaxial system is two. The exposure time was 200 ms with the EMCCD camera multiplication gain set to 3000 for all images. The incident laser power was adjusted before acquisition such that the brightest image in the $\psi$-stack was just below the camera saturation levels in the camera preview mode. Immediately after pTIRFM acquisition, a 20 $\times$ 20 $\mu$m AFM image of the central area within the same TIR illuminated ROI was acquired. Smaller AFM scans of the same area were acquired as necessary. All AFM images were captured in tapping-mode in aqueous pH 7.4 HEPES buffer using short-thin 125 $\mu$m V-shaped DNPS tips (Nanoprobes, Veeco) driven at a tip oscillation frequency of ~8.5 kHz, and a drive amplitude setpoint of 0.3 V. All AFM images were acquired as 512 $\times$ 512 pixel images at a scan rate of 1 Hz. All experiments were performed at room temperature. All AFM images were subjected to a zero-order flatten and an *x* axis second-order plane fit filter using Digital Instruments Nanoscope IIIa software (Ver. 5.30r1). The pTIRFM order parameter images were calculated using an in-house-written National Institutes of Health ImageJ (http://rsb.info.nih.gov/ij/, Ver. 1.41f) macro that is available upon request (95). The macro accepts a pTIRFM $\psi$-stack, the laser angle of incidence ($\alpha$), and the substrate/sample relative index of refraction ($n$) as inputs ($\alpha = 60°$ and $n = 0.84$ for these experiments). The plug-in then subtracts the background, determines $\psi_0$ by inspection, normalizes all *ij* pixels in the pTIRFM $\psi$-stack, and calculates factor $B$ at each *ij* pixel ($B_{ij}$) using a least-squares numerical algorithm. For each $B_{ij}$, $\langle P_2 \rangle_{ij}$ is evaluated and plotted in a new image. The order parameter image is color-coded using ImageJ's 8-bit FIRE lookup table. Order parameter images were analyzed using ImageJ's built-in image histogram and image threshold functions. The pTIRFM analysis was always restricted to the centermost homogenous region of the TIRF illumination ROI, matching the 20 $\times$ 20 $\mu$m area imaged by the AFM to avoid both analyzing pixels with low pTIRFM signal/noise ratios and compensating for spatial inhomogeneities at the boundary of the TIRF illumination profile.

## Materials and lipid bilayer preparation

A list of vendor product numbers for the materials listed here can be found in online Supporting Material. Dioleoylphosphatidylcholine (DOPC; 18:1), distearoylphosphatidylcholine (DSPC; 18:0), and cholesterol were purchased from Avanti Polar Lipids (Alabaster, AL). 1,1′-dieicosanyl-3,3,3′,3′-tetramethylindocarbocyanine perchlorate (DiI-$C_{20}$) was purchased from Molecular Targeting Technologies (Westchester, PA). 2-(4,4-difluoro-5,7-dimethyl-4-bora-3a,4a-diaza-*s*-indacene-3-pentanoyl)-1-hexadecanoyl-*sn*-glycero-3-phosphocholine (BODIPY-PC) was purchased from Molecular Probes (Eugene, OR). For chemical structures of molecules used in this study, see Fig. 2. Tetramethylrhodamine-5-isothiocyanate (TRITC) used in the pTIRFM calibration experiments was purchased from Molecular Probes. Stock solutions of lipid/cholesterol and dye in chloroform were prepared at 10 mg/mL and 1 mg/mL, respectively. Membrane bilayers were prepared by vesicle fusion (96) onto freshly cleaved grade V-1 muscovite mica sheets (SPI, West Chester, PA) using the method described previously (97). Substrates were secured in an Attofluor open well chamber (Invitrogen Canada, Burlington, Ontario, Canada) and held rigidly in a magnetic holder to the microscope stage.

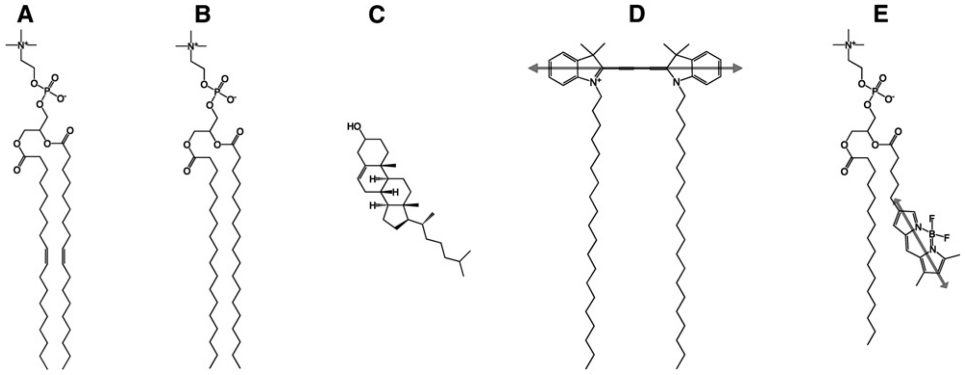


FIGURE 2 Chemical structures of the molecules used in model lipid bilayer experiments of this study. (*A*) DOPC. (*B*) DSPC. (*C*) Cholesterol. (*D*) DiI-$C_{20}$. (*E*) BODIPY-PC. The location and orientation of the transition dipole moments are indicated by double-ended arrows.

DiI-$C_{20}$ and BODIPY-PC were chosen as lipid order-sensing probes in this preliminary study for several reasons:

1. DiI has been used to image lateral heterogeneity in model and cellular membranes (98).
2. DiI-$C_{20}$ and BODIPY-PC partition unequally between different membrane phases, and both fluorescent probes were used to solve the DOPC/DSPC/cholesterol phase diagram (23,62,64).
3. Both probes possess a well-defined transition dipole moment, and as a result exhibit strong photoselection when illuminated with polarized light.
4. The orientation of DiI and BODIPY-PC in giant unilamellar vesicles (GUVs) has been studied previously using fluorescence polarization microscopy (FPM) (65,66,73,75), confirming that the transition dipole moments of DiI-$C_{20}$ and BODIPY-PC are oriented roughly perpendicular and parallel to the bilayer normal, respectively.
5. DiI-$C_{20}$ and BODIPY-PC probe the orientational order of different regions of the lipid bilayer. Specifically, DiI addresses the motional freedom of the lipid headgroups while BODIPY-PC provides insights into the local order of the lipid acyl chains.

## pTIRFM calibration

Calibration experiments designed to detect and correct for dichroism in the microscope optics involved performing pTIRFM imaging of randomly oriented fluorophores in solution near the TIR interface (1 $\mu$g/mL TRITC in ethanol on clean 170-$\mu$m-thick glass coverslips). For a randomly oriented fluorescent species and in the absence of instrument dichroism, $\langle P_2 \rangle$ should theoretically equal zero and $\langle \theta_c \rangle$ (Eq. 18) would be the magic-angle value of 54.7° (80). In our calibration experiments, we measured a pixel-average $\langle P_2 \rangle = 0.015 \pm 0.009$ ($\langle \theta_c \rangle = 54.2° \pm 0.4°$), indicating a negligible instrument bias ($f(\theta) \sim 1$, Appendix A)) (Fig. 3). As a result, no polarization corrections were made to the raw pTIRFM images.

At the end of each experiment, the optical microscope was switched into polarized epifluorescence mode and the excitation beam polarization was rotated 180° to check for in-plane azimuthal (parallel to the membrane surface) sample dichroism. In all experiments, no such dichroism was noted, confirming that the in-plane component of the fluorophore absorption dipole distribution was randomly oriented about the membrane normal (uniaxially symmetric) on the timescale of the experiment and thus the applicability of Eq. 2.

## RESULTS

To demonstrate the capabilities of our pTIRFM/AFM platform, we characterized the topography and local order of two different fluorescent lipid analogs incorporated into mica-supported lipid bilayers composed of DOPC, DSPC, and varying amounts of cholesterol. The phase diagram of this ternary mixture was solved recently, revealing several composition-dependent regions of macroscopic immiscibility (23). Generally, the addition of cholesterol to a solid ordered ($S_o$) lipid phase composed of lipids with saturated acyl chains increases the lateral mobility of the lipids and decreases the orientational order of the acyl chains to create a liquid-ordered state ($L_o$). Conversely, the addition of cholesterol to a liquid-disordered lipid phase ($L_d$) composed of lipids with at least one or more unsaturated bonds in the acyl chains decreases the lateral mobility and increases orientational order. The ordering and phase separation behavior of ternary mixtures of saturated lipids, unsaturated

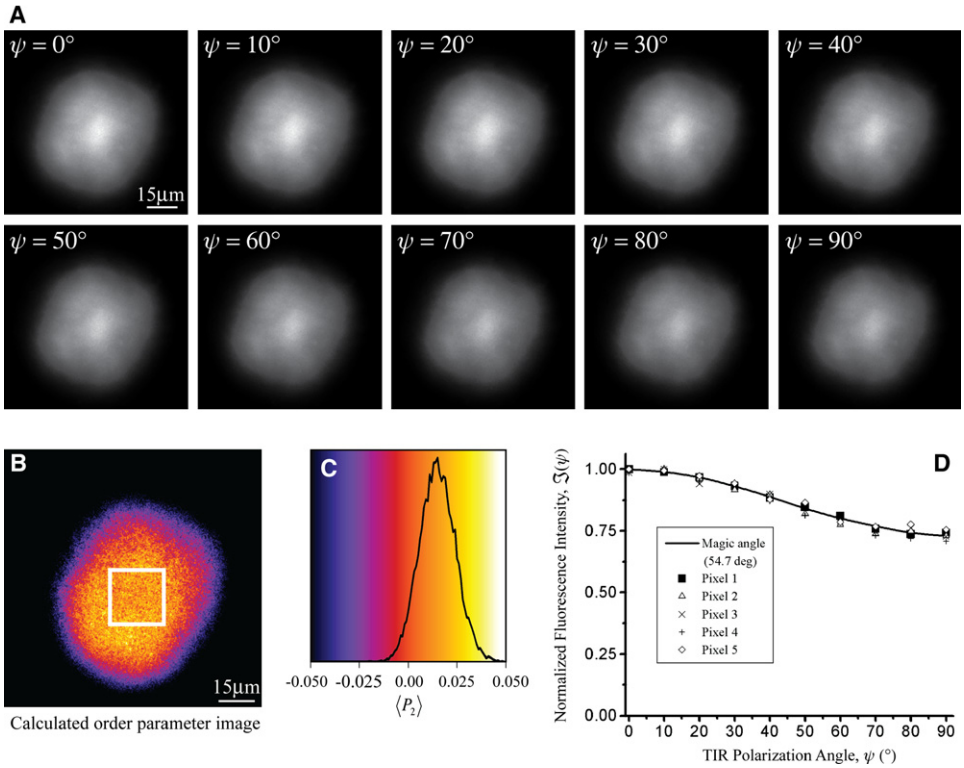


FIGURE 3 Calibration of the polarized TIRF microscope. (*A*) A $\psi$-image stack of a randomly oriented, dilute solution of TRITC dye molecules dissolved in ethanol (532 nm excitation). The image contrast settings are the same for these images allowing the gradual decrease in fluorescence intensity as $\psi$ is increased from 0° to 90° to be visualized. The intensity spatial distribution of these images reflects the nearly Gaussian-shaped profile ($TEM_{00}$ mode) of the TIRF illumination spot. (*B*) Calculated order parameter image of the $\psi$-image stack in panel *A*. This image is colored according to the color scale in the image histogram shown in panel *C*. The plotted image histogram is restricted to the 20 × 20 $\mu$m region of interest in panel *B*. The histogram is peaked close to the expected value of $\langle P_2 \rangle = 0$ for a random distribution of fluorophore absorption dipoles. (*D*) The normalized fluorescence intensity of five random pixel positions from the central-most region of the illumination spot in the $\psi$-image stack in panel *A* are plotted against the theoretical curve (*solid line*, Eq. 13; $\langle \theta_c \rangle = 54.7°$, $\langle P_2 \rangle = 0, B = 0.27$) expected for a random distribution of dye molecules when imaged by the pTIRFM technique. The good agreement between the measured points and the theoretical curve indicates that it is valid to calculate the order parameter on a single pixel level and that the pTIRFM technique can be measured with diffraction-limited spatial resolution.

lipids, and cholesterol are, however, not as clearly defined or predictable (23).

Correlated pTIRFM-AFM imaging of a 1:1 DOPC/DSPC/30 mol % cholesterol/1 mol % BODIPY-PC lipid bilayer revealed clear evidence of lipid phase separation into well-defined micron-sized domains (Fig. 4). From the pTIRFM $\psi$-image stack, the fluorescence intensity was greater in both membrane phases when illuminated with *p*-polarized light ($\psi = 0°$) as compared to illumination with *s*-polarized light ($\psi = 90°$). Qualitatively, this suggests that the absorption transition dipole moment of BODIPY-PC was largely oriented parallel to the membrane normal, in agreement with previous studies in GUVs (73,75). The AFM images of these same regions revealed that the dark domains in the fluorescence images were ~1 nm lower than their surroundings, suggesting that they are likely composed of DOPC. We attribute this topographical difference to variations in lipid-order and acyl-tail packing between DOPC and DSPC, with the DSPC lipids adopting a more ordered arrangement. The pTIRFM order parameter image, based on the BODIPY-PC signal, confirmed this difference in localized membrane order with the lower domains exhibiting a $\langle P_2 \rangle_{low}$ value of $0.218 \pm 0.029$ with a corresponding $\langle \theta_c \rangle_{low} = 46.2° \pm 1.1°$. In the surrounding taller phase, the corresponding $\langle P_2 \rangle_{high}$ and $\langle \theta_c \rangle_{high}$ values were $0.302 \pm 0.023$ and $43.0° \pm 0.9°$, respectively. The error in these measurements was determined by the standard deviation of the $\langle P_2 \rangle$ pixel values thresholded over the low and high topography regions in the order parameter image.

The same lipid mixture when doped with 1 mol % DiI-$C_{20}$ exhibited a similar morphology; however, the pTIRFM $\psi$-image stack showed greater fluorescence intensity in both phases when illuminated with *s*-polarized light (Fig. 5). This result qualitatively suggested that the absorption dipole moment of DiI-$C_{20}$ was oriented mostly perpendicular to the membrane normal, in agreement with the findings of other FPM studies (65,66,99) and suggestive of a motif wherein its two alkyl side chains are inserted into the membrane. Our assignment of this orientation was further supported by the negative order parameters measured for both the low and high topography membrane regions ($\langle P_2 \rangle_{low} = -0.348 \pm 0.011$; $\langle \theta_c \rangle_{low} = 71.1° \pm 0.7°$; $\langle P_2 \rangle_{high} = -0.383 \pm 0.005$; and $\langle \theta_c \rangle_{high} = 74.8° \pm 0.4°$). The difference in the DiI-$C_{20}$ order parameters is likely a consequence of differences in the lateral packing of the lipids within these different regions caused by the presence of and interaction with cholesterol.

We then examined the effect of cholesterol concentration on orientational order in the DOPC/DSPC model membrane system by examining changes in $\langle P_2 \rangle$ values (Fig. 6). Each point represents the average $\langle P_2 \rangle$ value determined from >1000 pixels from regions of interest in an order parameter image that were identified as either low or high topography in the corresponding AFM image. In the case of DOPC/DSPC/cholesterol membranes containing 1 mol % DiI-$C_{20}$, $\langle P_2 \rangle$ for both the high and low domains decreased linearly with increasing cholesterol concentration; however, in the case of the DOPC/DSPC/cholesterol membranes containing 1 mol % BODIPY-PC, the $\langle P_2 \rangle$ values in the high and low topography regions

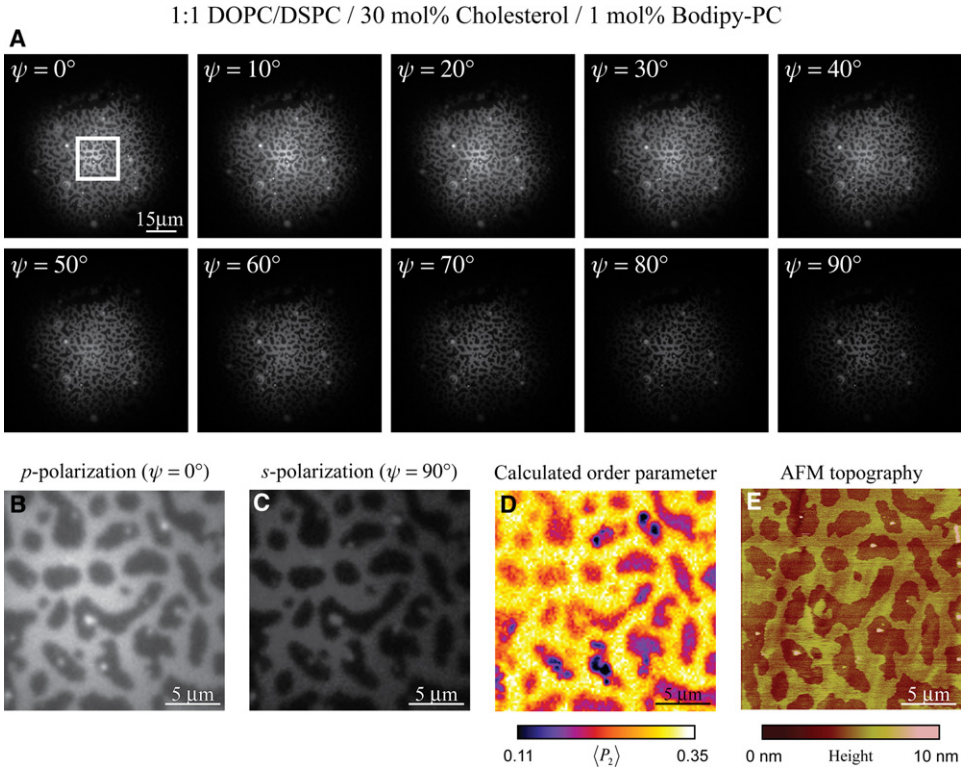


FIGURE 4 Representative pTIRFM/AFM image set of a (1:1) DOPC/DSPC/30 mol % Cholesterol/1 mol % BODIPY-PC lipid bilayer at room temperature. (*A*) The $\psi$-image stack showing the gradual decrease in image intensity as the evanescent field polarization angle is increased from 0° to 90°. Panels *B* and *C* compare the *p*- and *s*-polarized images of the 20 × 20 $\mu$m region enclosed by the open square in the first frame of panel *A*. (*D*) Calculated order parameter image of this same region. The very low order parameter spots in this image (*solid*) are unfused lipid vesicles that are also visible in the corresponding AFM topography image (*E*).

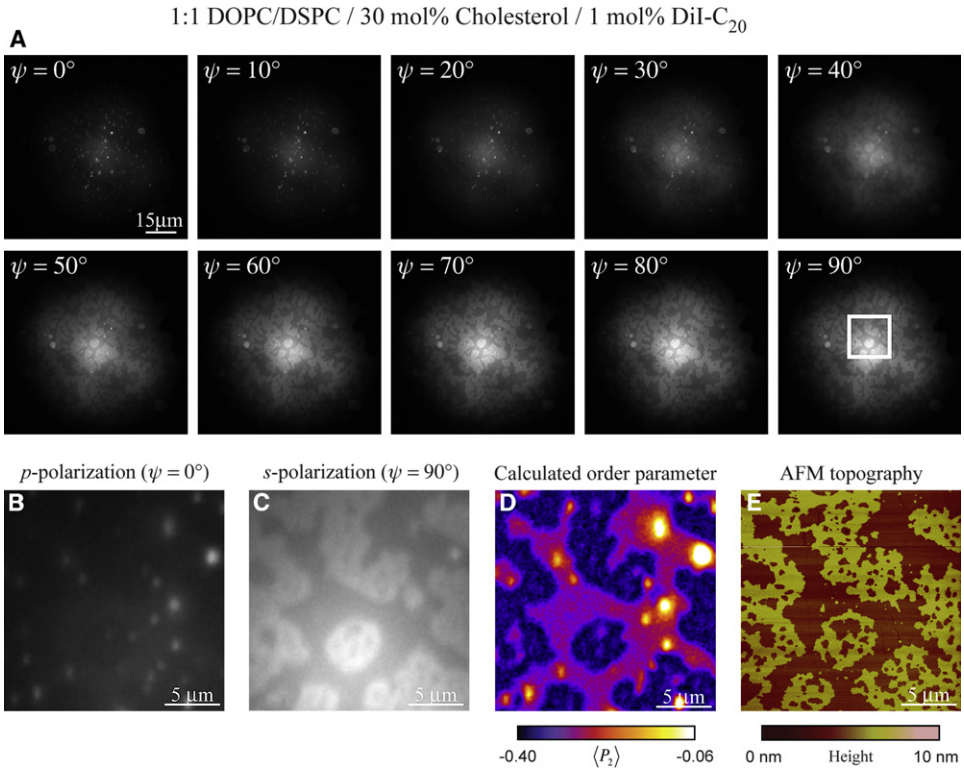


FIGURE 5 Representative pTIRFM/AFM image set of a (1:1) DOPC/DSPC/30 mol % Cholesterol/1 mol % DiI-$C_{20}$ lipid bilayer at room temperature. (*A*) The $\psi$-image stack showing the gradual increase in image intensity as the evanescent field polarization angle is increased from 0° to 90°. Panels *B* and *C* compare the *p*- and *s*-polarized images of the 20 × 20 $\mu$m region enclosed by the open square in the last frame of panel *A*. (*D*) Calculated order parameter image of this same region. The bright spots with an order parameter close to zero (*open*) are unfused lipid vesicles (also visible in *B*) that were swept away by the raster scanning motion of the AFM tip and subsequently do not appear in the corresponding AFM topography image (*E*).

exhibited opposite trends with cholesterol concentration, with a local maximum value of $\langle P_2\rangle_{low}$ and a local minimum value for $\langle P_2\rangle_{high}$ at the intermediate cholesterol concentration of 15 mol %.

Domain morphology was also dependent on cholesterol concentration. With 30% cholesterol, the BODIPY-PC doped DOPC/DSPC bilayers were populated by smooth, contiguous taller domains surrounding smaller irregularly shaped lower domain islands. This same morphology was seen for the DiI-$C_{20}$ doped DOPC/DSPC bilayers; however, the taller domains were less well-defined and appeared fragmented (Fig. 5). We would note that these features were also readily resolved by pTIRFM.

In the case of the 15 mol % cholesterol compositions, close inspection of the taller domains by AFM revealed that they were not contiguous but rather comprised closely packed collections of smaller (<250 nm in diameter) round tall domains interspersed with lower topography domains (Fig. 7). These morphologies were present for both the DiI-$C_{20}$ and BODIPY-PC doped cases. However, while these features were readily resolved by AFM, they were not observed by pTIRFM due to their subdiffraction limited size. Section analysis revealed that the height difference between the interspersed lower domains and the taller surrounding domains was ~1.5 nm, while the difference was ~1.2 nm between the taller domains and the surrounding lower phase domains (Fig. 7 *F*). This particular composition is very close to a tie line in the ternary phase diagram for DOPC/DSPC/cholesterol, bordering on a region that contains three distinct lipid phases (62,64). It is possible that these interspersed lower domains within the taller domains are the putative third phase that has been observed macroscopically in fluorescently labeled GUVs. These observations suggest careful interpretation of $\langle P_2\rangle$. Since we have shown that $\langle P_2\rangle$ can be domain- or phase-dependent, it should be viewed as a composite value incorporating order parameters associated with all domains located within the diffraction-limited ROI. This strongly suggests that one must be cautious in assuming that the ROI is homogeneous. Our correlated pTIRFM/AFM approach provides an excellent means of addressing the issue of heterogeneity within the diffraction-limited ROI. This is particularly important in cases where the reporter molecule, such as DiI-$C_{20}$, may partition into multiple phases.

Occasionally defects in the supported bilayer made it possible to resolve the supporting mica substrate (Fig. 7 *D*). Within these defects, small ~10-nm diameter lipid islands were resolved by AFM. A $\langle P_2\rangle_{defect}$ value of $-0.220 \pm 0.020$ was obtained in these regions, suggesting a more disordered distribution of DiI-$C_{20}$ absorption dipole orientations relative to that seen on the larger membrane patches. This is not unexpected, as these islands likely represent some intermediate state between a contiguous, cohesive, planar bilayer and a freely floating vesicle. This observation further supports the use of the correlated pTIRFM/AFM approach since the $\langle P_2\rangle_{defect}$ value is obtained from diffraction-limited region of interests holding both small DiI-$C_{20}$-containing lipid islands and bare, unlabeled mica.

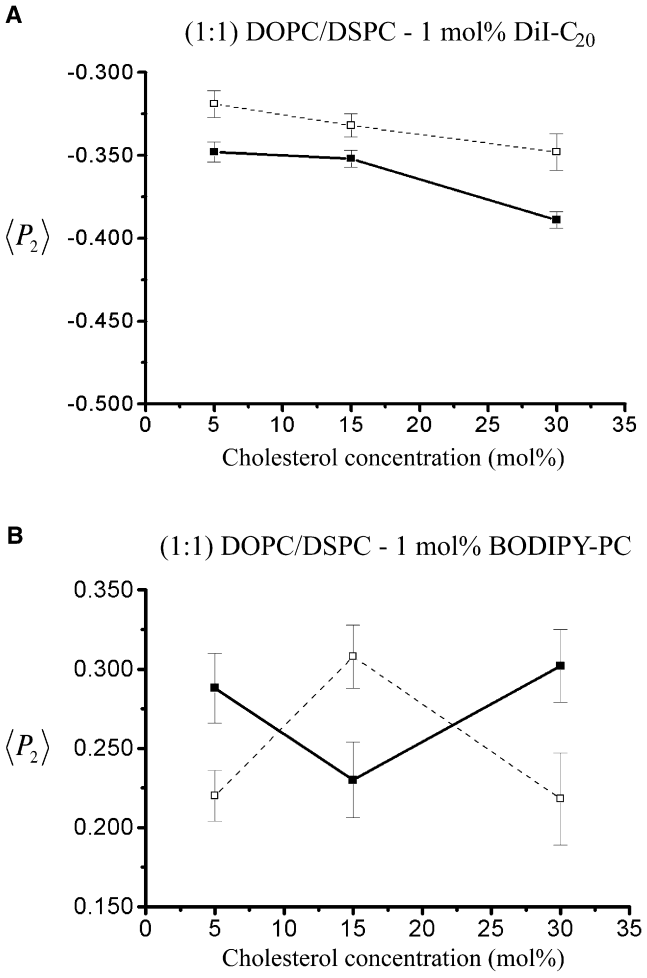


FIGURE 6 Summary data for pTIRFM/AFM bilayer experiments containing various amounts of cholesterol (5, 15, and 30 mol %). (*A*) (1:1:x) DOPC/DSPC/Cholesterol bilayers labeled with DiI-$C_{20}$. (*B*) (1:1:x) DOPC/DSPC/Cholesterol bilayers labeled with BODIPY-PC. (*Solid squares*) pTIRFM order parameter values associated with high topography membrane regions. (*Open squares*) pTIRFM order parameter values associated with low topography membrane regions. Each measured point in the graphs is an average of at least 1000 pixels averaged over the appropriate topography regions in a 20 × 20 $\mu$m pTIRFM order parameter image. The error bar for each point is determined by the standard deviation of measured pixel values around the average.

## DISCUSSION

Lipidomics research is focused on understanding how lipid composition influences membrane protein behavior, structure, and dynamics, and their effect on cellular activity (100). It is therefore important to develop tools and techniques that can follow these changes. The proof-of-concept experiments reported here demonstrate that a coupled imaging platform (pTIRFM/AFM) can resolve not only the partitioning of lipids and fluorescent probes into segregated two-dimensional domains, but also directly measure orientational order in these domains.

Our pTIRFM/AFM experiments with model DOPC/DSPC/cholesterol membranes labeled with either DiI-$C_{20}$ or BODIPY-PC have demonstrated that this technique can provide spatially resolved insights into molecular orientation in model membranes. The positive pTIRFM order parameter measured for samples labeled with BODIPY-PC are indicative of a time-averaged dipole orientation that is mostly parallel to the membrane normal, as would be expected for an acyl-chain-labeled lipid analog. Conversely, the samples labeled with DiI-$C_{20}$ displayed a negative pTIRFM order parameter, which is consistent with a dipole orientation that is mostly perpendicular to the membrane normal. Estimates of the static tilt angle of the probe's absorption dipole ($\langle\theta_c\rangle$), are in good agreement with previous FPM studies of these reporters in GUVs. A recent all-atom molecular dynamics simulation of 1,1′-dioctadecyl-3,3,3′,3′-tetramethylindocarbocyanine perchlorate (DiI-$C_{18}$) in a free-standing 1,2-dipalmitoyl-*sn*-glycero-3-phosphatidylcholine (DPPC; 16:0) bilayer revealed that the average tilt angle of the DiI-$C_{18}$ chromophore was 77 ± 17°, which is in good agreement with the tilt angles measured here by pTIRFM (101).

The fundamental role of cholesterol in biological membranes has been the subject of intense study for many years. Early model membrane studies focused on the effect of cholesterol in simple binary cholesterol/lipid mixtures. Before the lipid raft hypothesis, x-ray diffraction, NMR spectroscopy, fluorescence spectroscopy, and calorimetric experiments revealed that the addition of cholesterol to a pure saturated lipid membrane system generally reduced the order of the system whereas the addition of cholesterol to a pure unsaturated lipid membrane system has the opposite effect, increasing the order of the system to create the so-called liquid-ordered state (58–60). The lipid raft hypothesis and discovery of detergent-resistant membrane fractions in cells highlighted the importance of examining ternary lipid mixtures composed of saturated lipids, unsaturated lipids, and cholesterol (3–6). The ternary model membrane systems studied to date can be classified into one of two types (62,64) with the distinction between Type I and Type II being whether the domains can be observed by optical microscopy (Type II) or needed to be confirmed by other spectroscopic and imaging techniques (Type I). The phase diagrams of both types of ternary membrane mixtures are complex, exhibiting various combinations of liquid-disordered, liquid-ordered, and solid-ordered states. Modeling the phase behavior of these complex systems is contingent on data acquired using techniques capable of determining the various levels of order that are present (62).

The DOPC/DSPC/cholesterol membrane system is known to readily undergo macroscopic phase separation with changes in cholesterol concentration producing changes in membrane order. As we have shown, the measured steady-state pTIRFM order parameter reflects the order of the probe molecule and more specifically that of its chromophore and its location within the membrane. While these results are not surprising since the chromophores for DiI and BODIPY-PC reside in different parts of the membrane, the trends

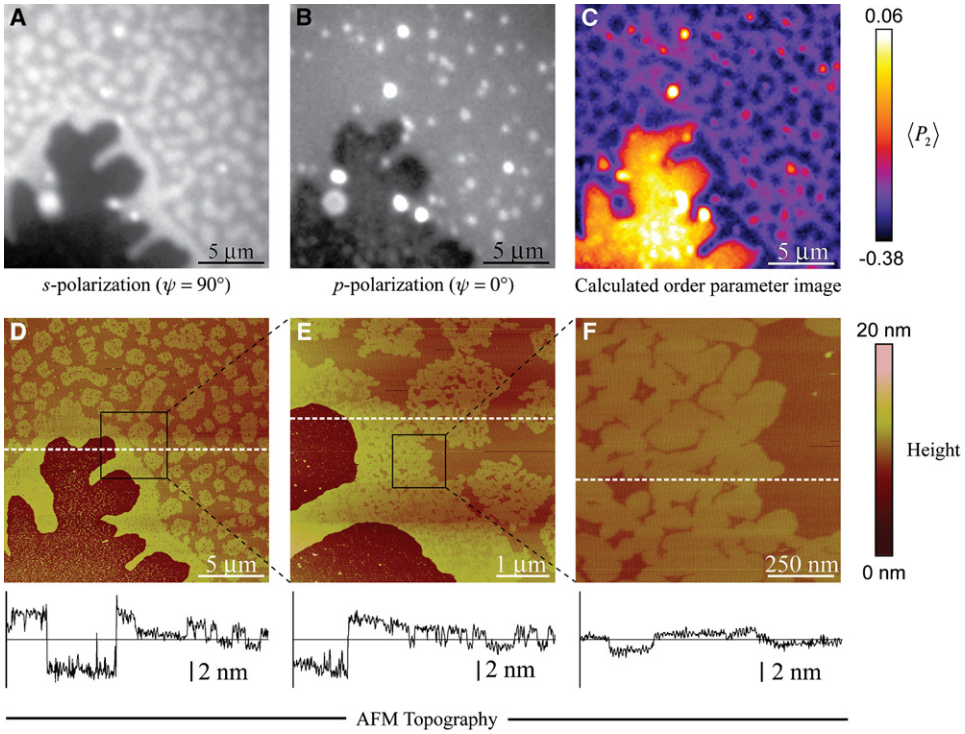


FIGURE 7 pTIRFM/AFM images of a 1:1 DOPC/DSPC/15 mol % cholesterol/1 mol % DiI-C20 lipid bilayer at room temperature. The *s*-polarized (*A*) and *p*-polarized (*B*) pTIRFM images. (*C*) Order parameter image. (*D*) AFM topography image of same field of view in the pTIRFM images. This image shows that the large dark feature in panels *A* and *B* is a membrane defect that exposes the mica substrate (~6 nm height difference). Panels *E* and *F* are smaller scanned AFM topography images of the boxed regions in panels *D* and *E*, respectively, and they reveal domain substructures that are not resolved optically. The dashed white lines in these AFM images correspond to the plotted height line profiles below the images. The bright spots over the membrane in the *p*-polarized image in panel *B* are unfused vesicles that are swept away by the raster-scanning motion of the AFM tip during imaging.

in order parameter as a function of cholesterol concentration are intriguing. The DiI-C20 results suggest that, with increasing cholesterol, the DiI chromophore becomes more horizontally rigid, lying parallel to the membrane plane in both the high and low topography phase-separated regions of the bilayer (Fig. 6 *A*). This trend is consistent with a loss of motional flexibility and increase in orientational order near the phospholipid headgroups, possibly due to the cholesterol's putative condensing or umbrella effect. In the case of BODIPY-PC, a decrease in acyl-chain order was noted for the high topography phase with a concomitant increase in acyl-chain order of the low topography phase as the cholesterol concentration increased from 5 to 15 mol % (Fig. 6 *B*). At 30 mol % cholesterol, the order parameters for both phases returned to their original 5 mol % cholesterol values. It is possible that this change in observed order parameter reflects the increase in the number of coexisting membrane phases predicted by the ternary phase diagram at this particular cholesterol loading.

These experiments serve to illustrate the challenges in relying solely on the spatial localization of fluorescent membrane probes as an indicator of a membrane's physical state. Partitioning of membrane probes such as DiI and BODIPY-PC has been shown to be dependent on the membrane lipid composition (77), and in some cases, the fluorescent label attached to membrane molecule (lipid or protein) can cause the molecule to alter its partitioning characteristics (97). Furthermore, as we have shown, the absolute fluorescent intensity of a labeled membrane phase can be strongly influenced by the photoselection effect and the orientational order of the fluorescent probe, especially in the case of planar-supported membrane bilayers. Conventional epifluorescence or confocal microscopy of these systems, even when unpolarized light is used, preferentially excites fluorescent molecules that are oriented with their absorption dipole oriented parallel to the membrane. The combination of pTIRFM and AFM can resolve these ambiguities since the pTIRFM order parameter and AFM topography data sets provide complementary and spatially correlated information. The mapping of membrane topography by AFM can help identify cases where subdiffraction limited domains are present, which will influence one's interpretation of the measured order parameter.

It is important to note that errors in the pTIRFM order parameter calculation can arise if there is rapid feature motion, such as diffusion of unfused vesicles, relative to the image acquisition time as this can cause problems with subsequent image manipulation. Furthermore, it has been reported that photooxidation of fluorescent probes can cause domains to appear and grow on the timescale of a few seconds (102), an effect seen in this work at very high, >50 mol % cholesterol concentrations. Care must be taken to examine image sets for these kinds of errors and exclude them from any statistical analysis of the calculated order parameter images. Another potential source of error in pTIRFM arises from the collection efficiency of the microscope objective and/or the anisotropic emission of polarized light from the fluorescent probes through the supported lipid bilayer substrate. While our calibration experiments revealed that this error was negligible, and within the uncertainty of

any given order parameter measurement, calibration experiments must always be performed to determine whether these effects dominate the measured fluorescence signals. If significant instrument or substrate dichroism is present, then a more rigorous analysis of the $F(\psi)$ curves that accounts for this bias must be performed (103).

Polarized TIRF microscopy of live cells has been demonstrated previously (81) using a prism-based TIRF microscope geometry (which is not compatible with AFM). In that publication, however, the formalism developed by Thompson et al. (80) was not implemented. In the former work (81), the authors focused on developing a method to visualize regions of the basal membrane of living cells that are undergoing blebbing or invagination during endocytosis or exocytosis. Instead of calculating a spatial map of the order parameter on the cell surface, the authors described generating a qualitative cell membrane orientation image as the ratio of *p*- to *s*-polarized images. Although an advantage of the order parameter is that it is model-independent and does not make any a priori assumptions about the fluorophore arrangement in relation to the membrane system, in the case of real cell membranes, the order parameter reflects a convolution of local order and local orientation of the membrane relative to the substrate. As long as the flatness of the cell membrane against the supporting substrate can be independently verified, the same analysis outlined in this article could be applied to determine the local order of the fluorescent probe. These limitations of cellular imaging have been discussed for polarized confocal imaging (70). Combined pTIRFM/AFM studies of live cells are further complicated by the fact that the AFM necessarily probes the apical side of the cell membrane while pTIRFM is restricted to the basal side of the cell membrane. Depending on the nature of the cell, and where on the cell one is interested in imaging, correlation of the AFM and pTIRFM signals may be difficult. We further note that the timescale differences present in the current application would exist in the case of pTIRFM/AFM imaging studies of live cells. As a raster-scanning and feedback-controlled imaging technique, AFM is necessarily slower than optical imaging. Live cell imaging by AFM can be challenging in general with video-rate AFM imaging being particularly difficult. A particularly compelling application of the combined pTIRFM/AFM imaging technique for live cell experiments would involve using the AFM to manipulate the apical membrane while observing basal membrane rearrangements and changes in probe order by pTIRFM.

## CONCLUSION

We have developed a coupled polarized objective-based TIRF-AFM platform and demonstrated its utility in analyzing the phase separation properties of ternary model membranes composed of saturated and unsaturated lipids and cholesterol. Having established that the combined pTIRFM/AFM imaging technique can directly interrogate the spatially heterogeneous orientational order of fluorescent probes embedded in phase-separated model membranes, it is now possible to extend the technique to more complex systems where the system under study is perturbed so that time-lapse changes in the probe's orientational order and membrane topography can be monitored. The ability to measure orientational and topographical dynamics associated with various raft-mediated phenomena, such as membrane remodeling due to the action of antimicrobial peptides, will provide a more complete picture of the molecular events associated with these activities, both in model and real cell membranes (14,22,26). While this work used fluorescent lipid analogs to infer orientational order, this technique can be readily applied to any fluorescently labeled proteins, provided a priori knowledge of the fluorophore linkage to the protein of interest is available (103,104). The imaging system described here can be readily expanded to include fluorescence resonance energy transfer and fluorescence correlation spectroscopy capabilities by adding the appropriate color and/or polarization filters (105,106).

## APPENDIX A: REVIEW OF pTIRFM IN UNIAXIALLY SYMMETRIC SYSTEMS

At the TIR substrate-sample interface, evanescent wavefronts propagate horizontally along the surface in a direction defined as the *x* axis. A right-handed Cartesian coordinate system is formed from a direction such that the *z* axis lies parallel to the interface normal and points away from the interface into the lower refractive index medium $n_1$. Under pTIRFM illumination, rotating $\psi$ causes the evanescent wave electric field vector to rotate from a direction linearly polarized parallel to the interface (*s*-polarization, $\psi = 90°$) to a direction that is linearly polarized mostly perpendicular to the interface (*p*-polarization, $\psi = 0°$). These directional properties of the polarized evanescent wave can be understood by examining the explicit equation that represents the evanescent electric field vectors, $\mathbf{E}_{ew}$. Using complex notation, $\mathbf{E}_{ew}$ is written as (107,108)

$$\mathbf{E}_{ew} = \big(E_x(\cos\psi), E_y(\sin\psi), E_z(\cos\psi)\big)e^{-2z/d_p}e^{i(k_x x-\omega t)}, \tag{3}$$

where $\lambda_0$ is the vacuum wavelength of the exciting laser light, $k_x$ is the magnitude of the evanescent wave vector, and $d_p$ is the evanescent field penetration depth as described below:

$$k_x = \frac{2\pi n_2 \sin\alpha}{\lambda_0}, \tag{4}$$

$$d_p = \frac{\lambda_0}{4\pi\sqrt{n_2^2\sin^2\alpha - n_1^2}}. \tag{5}$$

The value $d_p$ characterizes the axial thickness of the evanescent field illumination profile, representing the distance over which the illumination intensity drops to $1/e$ of its strength at the interface from medium $n_2$. $E_x$, $E_y$, and $E_z$ are the directional components of the evanescent electric field vector and can be expressed in terms of $\alpha$ and the relative index of refraction $n = n_1/n_2$:

$$E_x = \frac{2\cos\alpha\big(\sin^2\alpha - n^2\big)^{1/2}}{\big(n^4\cos^2\alpha + \sin^2\alpha - n^2\big)^{1/2}}e^{-i(\delta_{\|}+\pi/2)}, \tag{6}$$

$$E_y = \frac{2\cos\alpha}{(1-n^2)^{1/2}} e^{-i(\delta_\perp)}, \quad (7)$$

$$E_z = \frac{2\cos\alpha\sin\alpha}{\left(n^4\cos^2\alpha + \sin^2\alpha - n^2\right)^{1/2}} e^{-i(\delta_\parallel)}, \quad (8)$$

where $\delta_\perp$ and $\delta_\parallel$ are phase factors relative to the incident light beam wavefronts from the $n_2$ medium below the TIR interface. Equations 3–8 show that an incident plane wave linearly polarized perpendicular ($\psi = 90°$) or parallel ($\psi = 0°$) to the plane of incidence gives rise to an evanescent electric field that is also polarized perpendicular or parallel, respectively, to the plane of incidence. However, while the perpendicular evanescent field (designated $\mathbf{E}_s$) is strictly linearly polarized in the $y$ direction, the parallel evanescent field (designated $\mathbf{E}_p$) has a polarization with components along both $z$ and $x$:

$$\mathbf{E}_s = E_y\hat{y}, \quad (9)$$

$$\mathbf{E}_p = E_x\hat{x} + E_z\hat{z}. \quad (10)$$

The $\mathbf{E}_p$ vectors cartwheel through the $xz$ plane as a function of coordinate $x$ and time $t$. $\mathbf{E}_p$ is more along $z$ than $x$, however, and at the critical angle, the $x$ component of the $p$-polarized electric field vanishes. The polarization characteristics of the evanescent field should be distinguished from those present in polarized epifluorescence microscopy. With polarized epifluorescence microscopy, the illuminating light beam traverses normal to the substrate-sample interface (parallel to the $z$ axis) and polarization is therefore restricted to the $xy$ plane.

A fluorescent molecule preferentially absorbs light when the polarization vector of the excitation light is parallel to the transition dipole moment of the molecule. Consider a single fluorescent molecule with a defined absorption transition dipole moment, $\boldsymbol{\mu}_{abs}$. For simplicity, we assume that the emission dipole is parallel to $\boldsymbol{\mu}_{abs}$. The single molecule is oriented in a flat lipid bilayer such that $\boldsymbol{\mu}_{abs}$ has polar angle $\theta$ and azimuthal angle $\phi$ with respect to the membrane normal. We assume that the bilayer is uniaxially symmetric, lying adjacent and parallel to the TIR interface on the lower index medium $n_1$ side. The probability of absorption of light by this single molecule, $A(\theta,\phi,\psi)$, when illuminated by a polarized evanescent wave is given by the squared scalar product of the vectors $\boldsymbol{\mu}_{abs}$ and $\mathbf{E}_{ew}$:

$$A(\theta,\phi,\psi) = \left\langle \left(\boldsymbol{\mu}_{abs} \cdot \mathbf{E}_{ew}\right)^2 \right\rangle. \quad (11)$$

The angled brackets in the above equation denote a time-average over the characteristic time associated with light absorption (picosecond range). In this work, we are not working at the single molecule level. Rather, the membranes are doped with many fluorescent probes (1 mol %) and thus any given region of interest in the sample contains a large collection of oriented fluorescent probes that can be mathematically represented by an orientation probability distribution function, $N(\theta,\phi)$. Since these probes are free to rotationally diffuse in the membrane, we expect the azimuthal angle of the probes in any region of interest of the membrane to be randomly distributed at any given moment in time (supporting experimental evidence for this assumption is provided in the section on pTIRFM calibration). $N(\theta,\phi)$ therefore depends only on the probes' polar angle distribution ($N(\theta,\phi)\rightarrow N(\theta)$) and can be mathematically described by a series expansion of orthogonal basis functions that also exhibit cylindrical symmetry. The associated Legendre polynomials, $P_l(\cos\theta)$, satisfy this condition and are the most logical choice of basis functions for the expansion, thus permitting the distribution to be expressed with the following normalization condition:

$$N(\theta) = \sum_{l=1}^{\infty} \langle P_l \rangle P_l(\cos\theta), \quad (12)$$

$$\int_0^{\pi} N(\theta)\sin\theta d\theta = 1. \quad (13)$$

The $\langle P_l \rangle$ values are weighting coefficients for each term in the infinite series and are sometimes referred to as model-independent order parameters. Equation 12 is of a general mathematical form and can be equally well applied to describe any distribution of oriented molecules or dipoles (of any type—electronic, vibrational, spin magnetic, etc.) that possess uniaxial symmetry. This equation is frequently encountered in the theories describing other orientation-sensitive biophysical techniques such as polarized attenuated total internal reflection Fourier transform infrared (pATR-FTIR) spectroscopy and nuclear magnetic resonance (NMR) spectroscopy.

The $\langle P_l \rangle$ order parameters are measurable quantities that can be interpreted to characterize the time- and ensemble-averaged structural order of the absorption dipole distribution in a defined detection volume. If the absorption dipoles in the detection volume change their direction significantly during the typical light absorption timescale of picoseconds, then $N(\theta)$ will also include a time average. Since pTIRFM is a light absorption/dichroism technique, its intrinsic timescale lies in the picosecond range, providing information about the instantaneous dipole orientation distribution in a detection volume, averaged over many transition cycles during the instrument sampling/exposure time (~200 ms in this work). When all $\langle P_l \rangle$ values are known, $N(\theta)$ is completely and uniquely identified. Unfortunately, most orientation-sensitive biophysical techniques are capable of measuring only a finite number of order parameters, usually only the first few up to rank $l = 2$ or $l = 4$ (the odd terms vanish for dipoles possessing bidirectional symmetry). On the other hand, the lower rank terms in the series are usually the most important and the higher rank terms can be truncated to yield an expression for $N(\theta)$ that approximates the real orientation distribution.

The raw steady-state fluorescence intensity signal as a function of the evanescent wave polarization angle, $F(\psi)$, is predicted to be proportional to the integrated sum of the absorption by a single fluorescent molecule weighted by the orientation probability distribution of all fluorescent molecules in the region of interest over all possible polar angles:

$$F(\psi) = 2\pi K \int_0^{\pi} N(\theta)A(\theta)f(\theta)\sin\theta d\theta, \quad (14)$$

where $K$ is a constant encapsulating various fluorescent probe parameters (molar extinction coefficient, quantum efficiency, probe concentration) and instrument efficiency factors (illumination intensity, detector sensitivity, etc.) that only affect the absolute value of $F(\psi)$. The quantity $f(\theta)$ is an orientation-dependent instrument correction factor that accounts for the fact that the NA of the objective is less than a solid angle of $2\pi$ and therefore never quite captures one-half of emitted fluorescence from a region of interest. The quantity $f(\theta)$ can also deviate from unity because large NA objectives can depolarize light that traverses through them (in either direction) (65,66) and also because the substrate can affect the angular spread of fluorescent light emitted from fluorophores with different polar orientations (80,109).

Substitution of Eqs. 9–11 into Eq. 14 and evaluation of the integral using the orthogonality property of the associated Legendre polynomials followed by normalization of the expression ($\Im(\psi)=F(\psi)/F(\psi_0)$) leads to Eq. 2. Parameter $B$ in Eq. 2 depends directly on the order parameters $\langle P_2 \rangle$ and $\langle P_4 \rangle$—all higher rank order parameters vanish after performing the integral (see Eq. 20 in (80)). Timbs and Thompson argued that when the effects of the microscope objective collection efficiency are sufficiently small ($f(\theta) \approx 1$), the dependence of $B$ on $\langle P_4 \rangle$ is weak, and thus a measurement of $B$ by pTIRFM gives a fairly accurate determination of $\langle P_2 \rangle$ alone (99). The expression for $B$ when $\langle P_4 \rangle = 0$ therefore reduces to Eq. 2 where

$$I_x = |E_x|^2 = E_x E_x^*, \quad (15)$$

$$I_y = |E_y|^2 = E_y E_y^*, \quad (16)$$

$$I_z = |E_z|^2 = E_z E_z^*. \quad (17)$$

The * symbol in Eqs. 15–17 denotes the complex conjugate operation.

## APPENDIX B: INTERPRETATION OF THE $\langle P_2 \rangle$ ORDER PARAMETER

By definition, the $\langle P_2 \rangle$ coefficient of the series expansion $N(\theta)$ is the average value of the $P_2(\cos\theta) = 1/2(3\cos^2\theta - 1)$ function over all polar angles of the dipoles in the orientation distribution, where $-0.5 \le \langle P_2 \rangle \le 1$. It is important to emphasize that the order parameter cannot provide an unambiguous determination of the inclination or motional freedom of the fluorescent probe dipoles since $\langle P_2 \rangle$ is only the first nontrivial coefficient in an infinite series of terms that make up $N(\theta)$ (Eq. 12). These limitations have been discussed in greater detail elsewhere (49,53,110). Nevertheless, the single $\langle P_2 \rangle$ order parameter that can be measured experimentally is a very useful quantitative model-independent indicator of the degree of order in a system. For example. $\langle P_2 \rangle = 1$ indicates complete ordering of all fluorophore dipoles along a direction parallel to the reference axis ($z$ axis) whereas, when $\langle P_2 \rangle = -0.5$, the dipoles are ordered perpendicular to the reference axis (but without any preferred azimuthal orientation within the plane perpendicular to the $z$ axis). A measured value of $\langle P_2 \rangle = 0$ suggests a randomly oriented distribution of dipoles since $\langle P_2 \rangle$ and all higher-ranking order parameters vanish for an isotropic arrangement of molecules. Values of $\langle P_2 \rangle$ between −0.5 and 0 or between 0 and 1 are usually interpreted to describe degrees of dipole ordering intermediate to these extremes. Since $\langle P_2 \rangle$ by itself cannot be used to formulate a complete determination of $N(\theta)$, one strategy has been to assume a physically plausible model of $N(\theta)$ for the system of interest and then interpret a measured value of $\langle P_2 \rangle$ in the context of this model. The simplest model assumes an infinitely narrow distribution (a delta function) of absorption dipoles centered at a polar angle $\theta_c$, in which case the $\langle P_2 \rangle$ order parameter is given by the following:

$$\langle P_2 \rangle = \frac{1}{2}\left(3\langle \cos^2\theta_c \rangle - 1\right). \quad (18)$$

When this model is used, the average tilt angle of the dipoles, $\langle \theta_c \rangle$, with respect to the $z$ axis can be calculated from an experimental evaluation of $\langle P_2 \rangle$. While the relationship between $\langle P_2 \rangle$ and $\langle \theta_c \rangle$ is nonlinear, it is monotonic and single-valued. Furthermore, it is only an accurate measure of dipole orientation when $\theta_c$ has a single steady-state uniform value throughout the sample. More complex models that account for dispersion about the tilt angle, such as the so-called wobble-in-a-cone model, have been developed to affix a more realistic meaning to the order parameter (80,99,111).

As has been discussed, the orientational order parameter $\langle P_2 \rangle$ only describes a single-valued unique orientation when $\langle P_2 \rangle = -0.5$ or 1. At all other intermediate values, the scalar $\langle P_2 \rangle$ value reflects a distribution of molecular orientations. Changes in $\langle P_2 \rangle$ may arise from changes in average molecular orientation, the distribution of molecular orientations about the average, or both. However, as has been emphasized by Burghardt, despite these limitations, the measured order parameter is still a intrinsic property of the system and provides real structural information about dipolar arrangements and motions (112). Burghardt further noted that model-independent order parameters should be measured to facilitate comparisons with other experimental approaches.

It is important to appreciate that, although the order parameter is an unequivocal scalar value measured with respect to an external director axis about which the molecules are symmetrically oriented, there may be a family of director axes for different types of motions. If the motions about these axes are independent of each other, then the measured order parameter can be represented as a product of individual contributions (49). It should also be emphasized that optical polarization methods like pTIRFM can only characterize the average orientation and the orientational freedom of the fluorophore's transition dipole moment. Relating this information to the overall orientation and motion of the parent molecule is nontrivial and it is not clear that the fluorophore's orientational order is necessarily reflective of that of the parent molecule and its local surroundings. Recently efforts have been underway to computationally evaluate orientational order (113–119). In the case of the fluorescent lipid analogue indocarbocyanine (DiI), molecular symmetry arguments can be used to roughly determine the orientation of the absorption transition dipole moment with respect to the molecule. Since DiI exhibits mirror symmetry, its hydrocarbon tails are parallel to the axis of symmetry halfway between them, and the conjugated bridge in the headgroup is perpendicular to the axis of symmetry (Fig. 2). The absorption and emission dipole angles must therefore exist as a symmetric pair with respect to the long axis of the conjugated bridge axis. Numerical calculation and time-resolved fluorescence anisotropy studies confirm that both transition dipoles lie nearly parallel to the bridge axis (81). A similar argument can be made for the other fluorescent probe used in this study, BODIPY-PC.

## APPENDIX C: THE FLUORESCENCE-DETECTED DICHROIC RATIO

What is the minimum number of images required to determine $\langle P_2 \rangle$ by pTIRFM? As is the case with most polarization-sensitive techniques, the minimum number of measurements is two, namely the two orthogonal components of the fluorescence intensity $F(\psi = 0^\circ)$ and $F(\psi = 90^\circ)$ (90). The advantage of measuring $F$ at several polarization angles is that it facilitates a more reliable fitting of the least-squares algorithm that is applied in the calculation of factor $B$ from experimental data. The tradeoff, of course, is that it requires more time to collect multiple images, which could lead to errors when the system is undergoing rapid changes in the distribution of probe orientations/order. The unnormalized form of Eq. 2 after performing the integral of Eq. 14 and dropping the numerical constant $2\pi K$ is given by (see Eqs. 15–17 in (80))

$$F(\psi) = a' + b'\cos^2\psi, \quad (19)$$

where

$$a' = I_y(1 - \langle P_2 \rangle), \quad (20)$$

$$b' = \left(I_z - I_y + I_x\right) + \langle P_2 \rangle \left(2I_z + I_y - I_x\right). \quad (21)$$

In analogy to the pATR-FTIR dichroic ratio, $R^{ATR}$ (50,53,110,120), which is defined as the ratio of the integrated intensity of a spectroscopic infrared absorption band, $A$, when excited with parallel ($s$-) and perpendicularly ($p$-) polarized infrared light,

$$R^{ATR} = \frac{A_{||}}{A_\perp}, \quad (22)$$

a similar quantity for pTIRFM, which we call the fluorescence-detected dichroic ratio $R^{FD}$, can be defined as

$$R^{FD} = \frac{F_p}{F_s} = \frac{F(\psi = 0^\circ)}{F(\psi = 90^\circ)} = 1 + \frac{b'}{a'} = 1 + \frac{\left(I_z - I_y + I_x\right) + \langle P_2 \rangle \left(2I_z + I_y - I_x\right)}{I_y(1 - \langle P_2 \rangle)}. \quad (23)$$

The equation above can be rearranged to create an explicit expression for $\langle P_2 \rangle$ in terms of $R^{FD}$:

$$\langle P_2 \rangle = \frac{I_x - R^{FD} I_y + I_z}{I_x - R^{FD} I_y - 2I_z}. \quad (24)$$

This expression for the pTIRFM order parameter is identical to the equation that defines the pATR-FTIR spectroscopy order parameter in terms of $R^{ATR}$

in the thin film approximation (50,110). Since pTIRFM is a spatially resolved technique, $R^{FD}$ can be calculated at each pixel in the image from the measured $F_p$ and $F_s$ images, yielding $R^{FD}_{ij}$. The above equation can then be used to calculate $\langle P_2 \rangle_{ij}$.

When the incident angle is set to the critical angle ($\alpha = \alpha_c$), $I_x = 0$, and $\langle P_2 \rangle$ reduces further to

$$\langle P_2 \rangle = \frac{R^{FD} I_y - I_z}{R^{FD} I_y + 2 I_z}. \quad (25)$$

If the numerator and denominator of the above equation are multiplied by $G = 1/R^{FD}$, the expression for $\langle P_2 \rangle$ takes on a more familiar form resembling the equation for fluorescence polarization anisotropy:

$$\langle P_2 \rangle = \frac{I_y - G I_z}{I_y + 2 G I_z}. \quad (26)$$

## SUPPORTING MATERIAL

A figure is available at http://www.biophysj.org/biophysj/supplemental/S0006-3495(09)00204-5.

J.O. acknowledges and thanks Dr. Thomas P. Burghardt for many insightful discussions about pTIRFM. The authors thank Chantal Blanchard and George Sakellaropoulos of Olympus Canada for the loan of the EMCCD camera.

Support for this work was from Natural Sciences and Engineering Research Council (PGS-D scholarship to J.O.) and the Canada Research Chairs program (to C.M.Y.).

## REFERENCES

1. Pike, L. J. 2006. Rafts defined: a report on the Keystone Symposium on lipid rafts and cell function. *J. Lipid Res.* 47:1597–1598.
2. Shimshic, E. J., and H. M. McConnell. 1973. Lateral phase separation in phospholipid membranes. *Biochemistry.* 12:2351–2360.
3. Simons, K., and E. Ikonen. 1997. Functional rafts in cell membranes. *Nature.* 387:569–572.
4. Brown, D. A., and E. London. 1998. Functions of lipid rafts in biological membranes. *Annu. Rev. Cell Dev. Biol.* 14:111–136.
5. Edidin, M. 2003. The state of lipid rafts: from model membranes to cells. *Annu. Rev. Biophys. Biomol. Struct.* 32:257–283.
6. Silvius, J. 2005. Lipid microdomains in model and biological membranes: how strong are the connections? *Q. Rev. Biophys.* 38:373–383.
7. Shaw, A. S. 2006. Lipid rafts: now you see them, now you don't. *Nat. Immunol.* 7:1139–1142.
8. Marguet, D., P. F. Lenne, H. Rigneault, and H. T. He. 2006. Dynamics in the plasma membrane: How to combine fluidity and order. *EMBO J.* 25:3446–3457.
9. Hancock, J. F. 2006. Lipid rafts: contentious only from simplistic standpoints. *Nat. Rev. Mol. Cell Biol.* 7:456–462.
10. Veatch, S. L. 2007. From small fluctuations to large-scale phase separation: lateral organization in model membranes containing cholesterol. *Semin. Cell Dev. Biol.* 18:573–582.
11. McConnell, H. M., L. K. Tamm, and R. M. Weis. 1984. Periodic structures in lipid monolayer phase-transitions. *Proc. Natl. Acad. Sci.USA-Phys. Sci.* 81:3249–3253.
12. Varma, R., and S. Mayor. 1998. GPI-anchored proteins are organized in submicron domains at the cell surface. *Nature.* 394:798–801.
13. Korlach, J., P. Schwille, W. W. Webb, and G. W. Feigenson. 1999. Characterization of lipid bilayer phases by confocal microscopy and fluorescence correlation spectroscopy. *Proc. Natl. Acad. Sci. USA.* 96:8461–8466.
14. Dietrich, C., L. A. Bagatolli, Z. N. Volovyk, N. L. Thompson, M. Levi, et al. 2001. Lipid rafts reconstituted in model membranes. *Biophys. J.* 80:1417–1428.
15. Khan, T. K., B. Yang, N. L. Thompson, S. Maekawa, R. M. Epand, et al. 2003. Binding of NAP-22, a calmodulin-binding neuronal protein, to raft-like domains in model membranes. *Biochemistry.* 42:4780–4786.
16. Kahya, N., D. Scherfeld, K. Bacia, and P. Schwille. 2004. Lipid domain formation and dynamics in giant unilamellar vesicles explored by fluorescence correlation spectroscopy. *J. Struct. Biol.* 147:77–89.
17. de la Serna, J. B., J. Perez-Gil, A. C. Simonsen, and L. A. Bagatolli. 2004. Cholesterol rules—direct observation of the coexistence of two fluid phases in native pulmonary surfactant membranes at physiological temperatures. *J. Biol. Chem.* 279:40715–40722.
18. Veatch, S. L., and S. L. Keller. 2005. Seeing spots: complex phase behavior in simple membranes. *Biochim. Biophys. Acta Mol. Cell Res.* 1746:172–185.
19. Lagerholm, B. C., G. E. Weinreb, K. Jacobson, and N. L. Thompson. 2005. Detecting microdomains in intact cell membranes. *Annu. Rev. Phys. Chem.* 56:309–336.
20. Meder, D., M. J. Moreno, P. Verkade, W. L. C. Vaz, and K. Simons. 2006. Phase coexistence and connectivity in the apical membrane of polarized epithelial cells. *Proc. Natl. Acad. Sci. USA.* 103:329–334.
21. Bagatolli, L. A. 2006. To see or not to see: lateral organization of biological membranes and fluorescence microscopy. *Biochim. Biophys. Acta Biomembr.* 1758:1541–1556.
22. Baumgart, T., A. T. Hammond, P. Sengupta, S. T. Hess, D. A. Holowka, et al. 2007. Large-scale fluid/fluid phase separation of proteins and lipids in giant plasma membrane vesicles. *Proc. Natl. Acad. Sci. USA.* 104:3165–3170.
23. Zhao, J., J. Wu, F. A. Heberle, T. T. Mills, P. Klawitter, et al. 2007. Phase studies of model biomembranes: complex behavior of DSPC/DOPC/cholesterol. *Biochim. Biophys. Acta Biomembr.* 1768: 2764–2776.
24. Esposito, C., A. Tian, S. Melamed, C. Johnson, S. Y. Tee, et al. 2007. Flicker spectroscopy of thermal lipid bilayer domain boundary fluctuations. *Biophys. J.* 93:3169–3181.
25. Cicuta, P., S. L. Keller, and S. L. Veatch. 2007. Diffusion of liquid domains in lipid bilayer membranes. *J. Phys. Chem. B.* 111: 3328–3331.
26. Montes, L. R., A. Alonso, F. M. Goni, and L. A. Bagatolli. 2007. Giant unilamellar vesicles electroformed from native membranes and organic lipid mixtures under physiological conditions. *Biophys. J.* 93:3548–3554.
27. Jacobson, K., O. G. Mouritsen, and R. G. W. Anderson. 2007. Lipid rafts: at a crossroad between cell biology and physics. *Nat. Cell Biol.* 9:7–14.
28. de Almeida, R. F. M., J. Borst, A. Fedorov, M. Prieto, and A. Visser. 2007. Complexity of lipid domains and rafts in giant unilamellar vesicles revealed by combining imaging and microscopic and macroscopic time-resolved fluorescence. *Biophys. J.* 93:539–553.
29. Crane, J. M., V. Kiessling, and L. K. Tamm. 2005. Measuring lipid asymmetry in planar supported bilayers by fluorescence interference contrast microscopy. *Langmuir.* 21:1377–1388.
30. Li, L., and J. X. Cheng. 2008. Label-free coherent anti-Stokes Raman scattering imaging of coexisting lipid domains in single bilayers. *J. Phys. Chem. B.* 112:1576–1579.
31. Kraft, M. L., P. K. Weber, M. L. Longo, I. D. Hutcheon, and S. G. Boxer. 2006. Phase separation of lipid membranes analyzed with high-resolution secondary ion mass spectrometry. *Science.* 313: 1948–1951.
32. Rice, J. H. 2007. Beyond the diffraction limit: far-field fluorescence imaging with ultrahigh resolution. *Mol. Biosyst.* 3:781–793.

33. O'Shea, P., M. Somekh, and W. Barnes. 2008. Shedding light on life. *Phys. World.* 21:29–34.
34. Axelrod, D., and G. M. Omann. 2006. Combinatorial microscopy. *Nat. Rev. Mol. Cell Biol.* 7:944–952.
35. Shaw, J. E., R. F. Epand, K. Sinnathamby, Z. G. Li, R. Bittman, et al. 2006. Tracking peptide-membrane interactions: insights from in situ coupled confocal-atomic force microscopy imaging of NAP-22 peptide insertion and assembly. *J. Struct. Biol.* 155:458–469.
36. Slade, A. L., J. S. Schoeniger, D. Y. Sasaki, and C. M. Yip. 2006. In situ scanning probe microscopy studies of tetanus toxin-membrane interactions. *Biophys. J.* 91:4565–4574.
37. Shaw, J. E., J. R. Alattia, J. E. Verity, G. G. Prive, and C. M. Yip. 2006. Mechanisms of antimicrobial peptide action: studies of indolicidin assembly at model membrane interfaces by in situ atomic force microscopy. *J. Struct. Biol.* 154:42–58.
38. Alattia, J. R., J. E. Shaw, C. M. Yip, and G. G. Prive. 2007. Molecular imaging of membrane interfaces reveals mode of $\beta$-glucosidase activation by saponin C. *Proc. Natl. Acad. Sci. USA.* 104: 17394–17399.
39. Trache, A., and G. A. Meininger. 2005. Atomic force-multi-optical imaging integrated microscope for monitoring molecular dynamics in live cells. *J. Biomed. Opt.* 10:1–17.
40. Lin, W. C., C. D. Blanchette, T. V. Ratto, and M. L. Longo. 2006. Lipid asymmetry in DLPC/DSPC-supported lipid bilayers: a combined AFM and fluorescence microscopy study. *Biophys. J.* 90:228–237.
41. Frankel, D. J., J. R. Pfeiffer, Z. Surviladze, A. E. Johnson, J. M. Oliver, et al. 2006. Revealing the topography of cellular membrane domains by combined atomic force microscopy/fluorescence imaging. *Biophys. J.* 90:2404–2413.
42. Chiantia, S., N. Kahya, J. Ries, and P. Schwille. 2006. Effects of ceramide on liquid-ordered domains investigated by simultaneous AFM and FCS. *Biophys. J.* 90:4500–4508.
43. Johnston, L. J. 2007. Nanoscale imaging of domains in supported lipid membranes. *Langmuir.* 23:5886–5895.
44. Shaw, J. E., R. F. Epand, J. C. Y. Hsu, G. C. H. Mo, R. M. Epand, et al. 2008. Cationic peptide-induced remodeling of model membranes: direct visualization by in situ atomic force microscopy. *J. Struct. Biol.* 180:563–578.
45. Hubbell, W. L., and H. M. McConnell. 1971. Molecular motion in spin-labeled phospholipids and membranes. *J. Am. Chem. Soc.* 93:314–326.
46. Seelig, A., and J. Seelig. 1974. Dynamic structure of fatty acyl chains in a phospholipid bilayer measured by deuterium magnetic-resonance. *Biochemistry.* 13:4839–4845.
47. Heyn, M. P. 1979. Determination of lipid order parameters and rotational correlation times from fluorescence depolarization experiments. *FEBS Lett.* 108:359–364.
48. Frey, S., and L. K. Tamm. 1991. Orientation of melittin in phospholipid-bilayers—a polarized attenuated total reflection infrared study. *Biophys. J.* 60:922–930.
49. Lafrance, C. P., A. Nabet, R. E. Prudhomme, and M. Pezolet. 1995. On the relationship between the order parameter $[P_2(\cos\theta)]$ and the shape of orientation distributions. *Can. J. Chem.* 73:1497–1505.
50. Citra, M. J., and P. H. Axelsen. 1996. Determination of molecular order in supported lipid membranes by internal reflection Fourier transform infrared spectroscopy. *Biophys. J.* 71:1796–1805.
51. Castanho, M., S. Lopes, and M. Fernandes. 2003. Using UV-Vis linear dichroism to study the orientation of molecular probes and biomolecules in lipidic membranes. *Spectrosc. J.* 17:377–398.
52. Dafforn, T. R., and A. Rodger. 2004. Linear dichroism of biomolecules: which way is up? Curr. Opin. Struct. Biol. 14:541–546.
53. Lopes, S., and M. Castanho. 2005. Overview of common spectroscopic methods to determine the orientation/alignment of membrane probes and drugs in lipidic bilayers. *Curr. Org. Chem.* 9:889–898.
54. Toptygin, G., and L. Brand. 1995. Determination of DPH order parameters in unoriented vesicles. *J. Fluoresc.* 5:39–50.
55. Gidwani, A., D. Holowka, and B. Baird. 2001. Fluorescence anisotropy measurements of lipid order in plasma membranes and lipid rafts from RBL-2H3 mast cells. *Biochemistry.* 40:12422–12429.
56. van Meer, G., D. R. Voelker, and G. W. Feigenson. 2008. Membrane lipids: where they are and how they behave. *Nat. Rev. Mol. Cell Biol.* 9:112–124.
57. Seelig, J., and W. Niederbe. 1974. Deuterium-labeled lipids as structural probes in liquid-crystalline bilayers—deuterium magnetic-resonance study. *J. Am. Chem. Soc.* 96:2069–2072.
58. Vist, M. R., and J. H. Davis. 1990. Phase-equilibria of cholesterol dipalmitoylphosphatidylcholine mixtures—$H^2$ nuclear magnetic-resonance and differential scanning calorimetry. *Biochemistry.* 29:451–464.
59. Ipsen, J. H., O. G. Mouritsen, and M. Bloom. 1990. Relationships between lipid-membrane area, hydrophobic thickness, and acyl-chain orientational order—the effects of cholesterol. *Biophys. J.* 57: 405–412.
60. Mouritsen, O. G., and M. Bloom. 1993. Models of lipid-protein interactions in membranes. *Annu. Rev. Biophys. Biomol. Struct.* 22: 145–171.
61. Lindblom, G., and G. Grobner. 2006. NMR on lipid membranes and their proteins. *Curr. Opin. Colloid Interface Sci.* 11:24–29.
62. Feigenson, G. W. 2006. Phase behavior of lipid mixtures. *Nat. Chem. Biol.* 2:560–563.
63. Veatch, S. L., O. Soubias, S. L. Keller, and K. Gawrisch. 2007. Critical fluctuations in domain-forming lipid mixtures. *Proc. Natl. Acad. Sci. USA.* 104:17650–17655.
64. Feigenson, G. W. 2007. Phase boundaries and biological membranes. *Annu. Rev. Biophys. Biomol. Struct.* 36:63–77.
65. Axelrod, D. 1979. Carbocyanine dye orientation in red-cell membrane studied by microscopic fluorescence polarization. *Biophys. J.* 26: 557–573.
66. Axelrod, D. 1989. Fluorescence polarization microscopy. *Methods Cell Biol.* 30:333–352.
67. Florine-Casteel, K. 1990. Phospholipid order in gel-phase and fluid-phase cell-size liposomes measured by digitized video fluorescence polarization microscopy. *Biophys. J.* 57:1199–1215.
68. Dix, J. A., and A. S. Verkman. 1990. Mapping of fluorescence anisotropy in living cells by ratio imaging—application to cytoplasmic viscosity. *Biophys. J.* 57:231–240.
69. Blackman, S. M., C. E. Cobb, A. H. Beth, and D. W. Piston. 1996. The orientation of eosin-5-maleimide on human erythrocyte band 3 measured by fluorescence polarization microscopy. *Biophys. J.* 71:194–208.
70. Benninger, R. K. P., B. Onfelt, M. A. A. Neil, D. M. Davis, and P. M. W. French. 2005. Fluorescence imaging of two-photon linear dichroism: cholesterol depletion disrupts molecular orientation in cell membranes. *Biophys. J.* 88:609–622.
71. Sot, J., L. A. Bagatolli, F. M. Goni, and A. Alonso. 2006. Detergent-resistant, ceramide-enriched domains in sphingomyelin/ceramide bilayers. *Biophys. J.* 90:903–914.
72. Li, L., and J. X. Cheng. 2006. Coexisting stripe- and patch-shaped domains in giant unilamellar vesicles. *Biochemistry.* 45:11819–11826.
73. Ariola, F. S., D. J. Mudaliar, R. P. Walvicka, and A. A. Heikal. 2006. Dynamics imaging of lipid phases and lipid-marker interactions in model biomembranes. *Phys. Chem. Chem. Phys.* 8:4517–4529.
74. Vrabioiu, A. M., and T. J. Mitchison. 2006. Structural insights into yeast septin organization from polarized fluorescence microscopy. *Nature.* 443:466–469.
75. Davey, A. M., R. P. Walvick, Y. X. Liu, A. A. Heikal, and E. D. Sheets. 2007. Membrane order and molecular dynamics associated with IgE receptor cross-linking in mast cells. *Biophys. J.* 92:343–355.
76. Greeson, J. N., and R. M. Raphael. 2007. Application of fluorescence polarization microscopy to measure fluorophore orientation in the outer hair cell plasma membrane. *J. Biomed. Opt.* 12:1–9.

77. Baumgart, T., G. Hunt, E. R. Farkas, W. W. Webb, and G. W. Feigenson. 2007. Fluorescence probe partitioning between $l_o/l_d$ phases in lipid membranes. *Biochim. Biophys. Acta Biomembr.* 1768:2182–2194.

78. Burghardt, T. P., K. Ajtai, D. K. Chan, M. F. Halstead, J. Li, and Y. Zheng. 2007. GFP-tagged regulatory light chain monitors single myosin lever-arm orientation in a muscle fiber. *Biophys. J.* 93: 2226–2239.

79. Davey, A. M., K. M. Krise, E. D. Sheets, and A. A. Heikal. 2008. Molecular perspective of antigen-mediated mast cell signaling. *J. Biol. Chem.* 283:7117–7127.

80. Thompson, N. L., H. M. McConnell, and T. P. Burghardt. 1984. Order in supported phospholipid monolayers detected by the dichroism of fluorescence excited with polarized evanescent illumination. *Biophys. J.* 46:739–747.

81. Sund, S. E., J. A. Swanson, and D. Axelrod. 1999. Cell membrane orientation visualized by polarized total internal reflection fluorescence. *Biophys. J.* 77:2266–2283.

82. Shaw, J. E., A. Slade, and C. M. Yip. 2003. Simultaneous in situ total internal reflectance fluorescence/atomic force microscopy studies of DPPC/dPOPC microdomains in supported planar lipid bilayers. *J. Am. Chem. Soc.* 125:11838–11839.

83. Shaw, J. E., J. Oreopoulos, D. Wong, J. C. Y. Hsu, and C. M. Yip. 2006. Coupling evanescent-wave fluorescence imaging and spectroscopy with scanning probe microscopy: challenges and insights from TIRF-AFM. *Surf. Interface Anal.* 38:1459–1471.

84. Hecht, E. 2002. Optics. Addison Wesley, San Francisco.

85. Axelrod, D. 1981. Cell-substrate contacts illuminated by total internal-reflection fluorescence. *J. Cell Biol.* 89:141–145.

86. Schmoranzer, J., M. Goulian, D. Axelrod, and S. M. Simon. 2000. Imaging constitutive exocytosis with total internal reflection fluorescence microscopy. *J. Cell Biol.* 149:23–31.

87. Axelrod, D. 2001. Total internal reflection fluorescence microscopy in cell biology. *Traffic.* 2:764–774.

88. Allersma, M. W., L. Wang, D. Axelrod, and R. W. Holz. 2004. Visualization of regulated exocytosis with a granule membrane probe using total internal reflection microscopy. *Mol. Biol. Cell.* 15:4658–4668.

89. Holz, R. W., and D. Axelrod. 2008. Secretory granule behavior adjacent to the plasma membrane before and during exocytosis: total internal reflection fluorescence microscopy studies. *Acta Physiol.* 192:303–307.

90. Lakowicz, J. 1999. Principles of Fluorescence Spectroscopy. Kluwer Academic/Plenum Publishers, New York.

91. Kliger, D. 1990. Polarized Light in Optics and Spectroscopy. Academic Press, Boston.

92. Johnson, S. J., T. M. Bayerl, D. C. McDermott, G. W. Adam, A. R. Rennie, et al. 1991. Structure of an adsorbed dimyristoylphosphatidylcholine bilayer measured with specular reflection of neutrons. *Biophys. J.* 59:289–294.

93. Koenig, B. W., S. Kruger, W. J. Orts, C. F. Majkrzak, N. F. Berk, et al. 1996. Neutron reflectivity and atomic force microscopy studies of a lipid bilayer in water adsorbed to the surface of a silicon single crystal. *Langmuir.* 12:1343–1350.

94. Pawley, J. 2006. Handbook of Biological Confocal Microscopy. Plenum Press, New York.

95. Collins, T. J. 2007. ImageJ for microscopy. *Biotechniques.* 43:25–30.

96. Brian, A. A., and H. M. McConnell. 1984. Allogeneic stimulation of cytotoxic T-cells by supported planar membranes. *Proc. Natl. Acad. Sci. USA Biol. Sci.* 81:6159–6163.

97. Shaw, J. E., R. F. Epand, R. M. Epand, Z. G. Li, R. Bittman, et al. 2006. Correlated fluorescence-atomic force microscopy of membrane domains: structure of fluorescence probes determines lipid localization. *Biophys. J.* 90:2170–2178.

98. Hao, M. M., S. Mukherjee, and F. R. Maxfield. 2001. Cholesterol depletion induces large scale domain segregation in living cell membranes. *Proc. Natl. Acad. Sci. USA.* 98:13072–13077.

99. Timbs, M. M., and N. L. Thompson. 1990. Slow rotational mobilities of antibodies and lipids associated with substrate-supported phospholipid monolayers as measured by polarized fluorescence photobleaching recovery. *Biophys. J.* 58:413–428.

100. van Meer, G. 2005. Cellular lipidomics. *EMBO J.* 24:3159–3165.

101. Gullapalli, R. R., M. C. Demirel, and P. J. Butler. 2008. Molecular dynamics simulations of DiI-$C_{18}$(3) in a DPPC lipid bilayer. *Phys. Chem. Chem. Phys.* 10:3548–3560.

102. Ayuyan, A. G., and F. S. Cohen. 2006. Lipid peroxides promote large rafts: effects of excitation of probes in fluorescence microscopy and electrochemical reactions during vesicle formation. *Biophys. J.* 91:2172–2183.

103. Forkey, J. N., M. E. Quinlan, and Y. E. Goldman. 2000. Protein structural dynamics by single-molecule fluorescence polarization. *Prog. Biophys. Mol. Biol.* 74:1–35.

104. Osborne, M. A. 2005. Real-time dipole orientational imaging as a probe of ligand-protein interactions. *J. Phys. Chem. B.* 109: 18153–18161.

105. Piston, D. W., and M. A. Rizzo. 2008. FRET by fluorescence polarization microscopy. *In* Fluorescent Proteins, 2nd edition Elsevier Academic Press, San Diego.

106. Kannan, B., J. Y. Har, P. Liu, I. Maruyama, J. L. Ding, et al. 2006. Electron multiplying charge-coupled device camera based fluorescence correlation spectroscopy. *Anal. Chem.* 78:3444–3451.

107. Axelrod, D., E. H. Hellen, and R. M. Fulbright. 1992. Total internal reflection fluorescence. *In* Topics in Fluorescence Spectroscopy., Vol. 3 J. R. Lakowicz, editor. Plenum Press, New York.

108. Flournoy, P. A., and W. J. Schaffers. 1966. Attenuated total reflection spectra from surfaces of anisotropic absorbing films. *Spectrochim. Acta.* 22:5–13.

109. Burghardt, T. P., and N. L. Thompson. 1984. Effect of planar dielectric interfaces on fluorescence emission and detection—evanescent excitation with high-aperture collection. *Biophys. J.* 46:729–737.

110. Axelsen, P. H., and M. J. Citra. 1996. Orientational order determination by internal reflection infrared spectroscopy. *Prog. Biophys. Mol. Biol.* 66:227–253.

111. Kinosita, K., S. Kawato, and A. Ikegami. 1984. Dynamic structure of biological and model membranes—analysis by optical anisotropy decay measurement. *Adv. Biophys.* 17:147–203.

112. Burghardt, T. P. 1984. Model-independent fluorescence polarization for measuring order in a biological assembly. *Biopolymers.* 23:2383–2406.

113. Stimson, L., L. Dong, M. Karttunen, A. Wisniewska, M. Dutka, et al. 2007. Stearic acid spin labels in lipid bilayers: insight through atomistic simulations. *J. Phys. Chem. B.* 111:12447–12453.

114. Loura, L. M. S., and J. P. P. Ramalho. 2007. Location and dynamics of acyl chain NBD-labeled phosphatidylcholine (NBD-PC) in DPPC bilayers. A molecular dynamics and time-resolved fluorescence anisotropy study. *Biochim. Biophys. Acta Biomembr.* 1768:467–478.

115. Curdova, J., P. Capkova, J. Plasek, J. Repakova, and I. Vattulainen. 2007. Free pyrene probes in gel and fluid membranes: perspective through atomistic simulations. *J. Phys. Chem. B.* 111:3640–3650.

116. Repakova, J., J. M. Holopainen, M. Karttunen, and I. Vattulainen. 2006. Influence of pyrene-labeling on fluid lipid membranes. *J. Phys. Chem. B.* 110:15403–15410.

117. Schroder, G. F., U. Alexiev, and H. Grubmuller. 2005. Simulation of fluorescence anisotropy experiments: probing protein dynamics. *Biophys. J.* 89:3757–3770.

118. Repakova, J., J. M. Holopainen, M. R. Morrow, M. C. McDonald, P. Capkova, et al. 2005. Influence of DPH on the structure and dynamics of a DPPC bilayer. *Biophys. J.* 88:3398–3410.

119. Bolterauer, C., and H. Heller. 1996. Calculation of IR dichroic values and order parameters from molecular dynamics simulations and their application to structure determination of lipid bilayers. *Eur. Biophys. J.* 24:322–334.

120. Tamm, L. K., and S. A. Tatulian. 1997. Infrared spectroscopy of proteins and peptides in lipid bilayers. *Q. Rev. Biophys.* 30:365–429.